Simple and robust synchrotron and laboratory solutions for high-resolution multimodal X-ray phase-based imaging

IOP Conf. Series: Journal of Physics: Conf. Series **849** (2017) 012040 doi:10.1088/1742-6596/849/1/012040

Simple and robust synchrotron and laboratory solutions for high-resolution multimodal X-ray phase-based imaging

M. Endrizzi[1], F.A. Vittoria[1], P.C. Diemoz[1], G.K. Kallon[1], D. Basta[1], A. Zamir[1], C.K. Hagen[1], U. H. Wagner[2], C. Rau[2], I.K. Robinson[3,4], A. Olivo[1,3]

[1] Department of Medical Physics and Biomedical Engineering, University College London, London WC1E 6BT, United Kingdom
[2] Diamond Light Source, Harwell Oxford Campus, Didcot OX11 0DE, United Kingdom
[3] Research Complex at Harwell, Harwell Oxford Campus, Didcot OX11 0FA, United Kingdom
[4] London Centre for Nanotechnology, London WC1H 0AH, United Kingdom

E-mail: m.endrizzi@ucl.ac.uk

Abstract. Edge illumination X-ray phase contrast imaging techniques are capable of quantitative retrieval of differential phase, absorption and X-ray scattering. We have recently developed a series of approaches enabling high-resolution implementations, both using synchrotron radiation and laboratory-based set-ups. Three-dimensional reconstruction of absorption, phase and dark-field can be achieved with a simple rotation of the sample. All these approaches share a common trait which consists in the use of an absorber that shapes the radiation field, in order to make the phase modulations introduced by the sample detectable. This enables a well-defined and high-contrast structuring of the radiation field as well as an accurate modelling of the effects that are related to the simultaneous use of a wide range of energies. Moreover, it can also be adapted for use with detectors featuring large pixel sizes, which could be desirable when a high detection efficiency is important.

1. Introduction

X-ray phase-contrast imaging (XPCI) enables incorporating phase information into the image formation process and subsequent image interpretation. This enhances and complements the capabilities of conventional radiography, which is based upon the absorption of X-ray radiation within the sample under study [1–3]. Among the various methods that have been developed over the years to enable XPCI [4–19], we focus here on edge illumination (EI) [20] which can be adapted for use with synchrotron radiation, microfocus and extended laboratory sources [21,22]. EI allows quantitative retrieval of attenuation, phase and scattering information [23,24] and offers high sensitivity and robustness against mechanical and thermal instabilities [25–29]. It can also be extended from planar to three-dimensional imaging, and also in that case deliver low doses to the specimen [30,31]. We report on and compare three experimental set-ups where a significant structuring of the X-ray beam by means of an attenuating mask enables simple and robust XPCI experiments, compatible with synchrotron radiation as well as X-ray beams generated with laboratory sources.

2. Methods

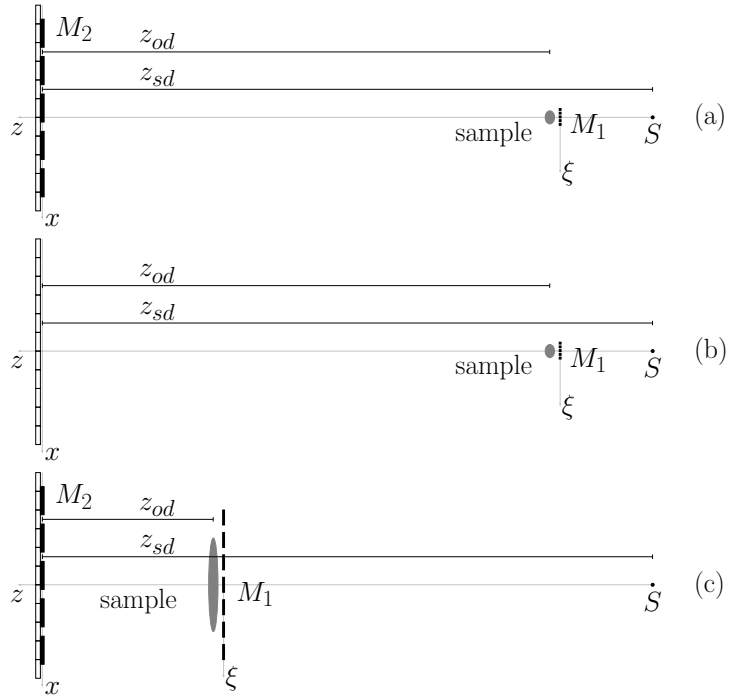

Figure 1: Sketch of the different experimental set-ups for edge-illumination XPCI, X-rays travel from right to left. (a) Laboratory high-resolution set-up: the sample mask is placed relatively close to the micrometre-sized focal spot. Magnification factor is about 10 in this configuration. Typical parameters: spot size $S = 3.5$ μm, $z_{sd} = 130$ cm and $z_{od} = 117$ cm [22]. The field of view is limited to millimitre-sized objects. (b) Laboratory beam tracking set-up: the detector mask can be removed and the modifications induced by the sample can be tracked by using groups of pixels [32]. (c) Low-magnification configuration where the sample mask is closer to the detector and an extended source can be used. Typical parameters: spot size $S = 70$ μm, $z_{sd} = 200$ cm and $z_{od} = 40$ cm [21]. The field of view allows for imaging of centimetre-sized objects.

In its synchrotron implementation, a typical EI imaging set-up consists of an absorbing slit that is placed immediately before the sample. When EI is translated to a laboratory set-up, the slit is usually replaced with a mask, a two-dimensional pattern alternating between transmitting and absorbing septa, and an extended area can be covered with a single exposure. This element spatially structures the beam and makes the phase shifts imparted by the object to the X-ray beam detectable. A second aperture, or mask, is placed before the detector with the function of analysing the X-ray beam after it has passed through the sample. This transforms the phase shift induced by sample into variations in the intensity recorded by each detector pixel.

Three examples are presented in Figure 1. The top panel (a) shows a high-resolution set-up operating with a tungsten anode laboratory source at 80 kVp [22], which enables micrometre-resolution X-ray phase imaging with a relatively compact design. The source size is about $S = 3.5$ μm and the sample mask is placed at 13 cm from it. Despite the use of a small focal spot, the coherence length $(z_{sd} - z_{od})\bar{\lambda}/\pi S \approx 0.4$ μm is small if compared to the characteristic lengths of the masks used in the experiment, which have typical periods of approximately 20 μm. The middle panel (b) presents a sketch of the beam tracking approach. This method can be implemented by removing the detector mask, and adapted to synchrotron radiation [33, 34]

as well as to laboratory microfocal X-ray tubes [32]. In the third panel (c) the most commonly used configuration is depicted. In this case, the geometrical magnification G is close to unity, which allows the use of an extended focal spot, typically in the range of $70 - 100$ μm. Also in this case, considering for example a molybdenum target at 40 kVp and $(z_{sd} - z_{od}) = 160$ cm, the coherence length is low, approximately 0.5 μm, and should be compared to mask periods in the range of $80 - 100$ μm. In terms of energy bandwidth, all these systems are achromatic [35] and fully exploit the wide spectrum produced by conventional laboratory X-ray tubes.

The illumination function describes how the detected intensity changes as a function of the relative displacement between the sample and the detector apertures. This intensity is maximum when the apertures are perfectly aligned, and progressively decreases with increasing misalignment. The typical working points are the two positions where the intensity is about 50% of the maximum. In these configurations the refraction induced by the sample translates into an increased or decreased detected intensity, depending on the combination of sign of refraction angle and slope of the illumination function. This can be used to quantitatively separate the sample's amplitude and phase, for example by using [36]:

$$I_{L,R} = \exp\left[-\int_{\mathcal{O}} \bar{\mu} dz\right] I_F(\Delta\xi_{1,2} - z_{od}\ \bar{\phi_x}/G) \tag{1}$$

where $\bar{\mu}$ is the linear attenuation coefficient, evaluated at the effective energy of the system. This energy is obtained by weighting each monochromatic component in the beam according to the source spectrum and the detector response [37, 38]. $\bar{\phi}_x = \partial\bar{\phi}/\partial x$ is the partial derivative of ϕ evaluated at the system's effective energy and I_F is the value of the illumination function the image has been acquired at. The integration is carried out over the spatial extension of the sample $\mathcal{O}$. The following two images are also defined $I_\Sigma = I_L + I_R$ and $I_\Delta = I_L - I_R$. It is important to note that the image I_Δ/I_Σ depends only on $\bar{\phi}_x$ and the experimental parameters, while I_Σ depends only on the sample's absorption [36].

In the beam tracking approach the effects of absorption T, refraction δx and scattering s are formulated as [33]:

$$I(x) = T I_0(x - \delta x) * s(x) \tag{2}$$

where I and I_0 are the intensity distributions acquired with and without the sample in the beam. With a high-resolution detector it is possible to resolve the intensity distributions corresponding to each pre-sample aperture that fits within the field of view. With this data, an over-constrained problem is formulated and the sample parameters are extracted through a non-linear fitting procedure, by comparing the shape of the intensity distributions recorded with and without the sample in the beam.

Equation 2 can also be used in the case of Figure 1(c), where the detector mask is present and a small geometrical magnification is used. By indicating the illumination and object function by L and O, respectively, and by representing them both through a multi-Gaussian model $L(x) = \sum_{n=1}^{N}(A_n/\sqrt{2\pi\sigma_n^2})\exp\left[-(x-\mu_n)^2/2\sigma_n^2\right]$ and $O(x) = \sum_{m=1}^{M}(A_m/\sqrt{2\pi\sigma_m^2})\exp\left[-(x-\mu_m)^2/2\sigma_m^2\right]$, the intensity recorded at the detector can be expressed as follows [24]:

$$\frac{I(x)}{I_0} = t\sum_m\sum_n A_{mn}\exp\left[-\frac{(x-\mu_{mn})^2}{2\sigma_{mn}^2}\right] \tag{3}$$

where $\mu_{mn} = \mu_m + \mu_n$, $\sigma_{mn}^2 = \sigma_m^2 + \sigma_n^2$ and $A_{mn} = A_m A_n(1/\sqrt{2\pi\sigma_{mn}^2})$. In many practical cases, a single Gaussian term is enough to accurately represent both L and O, and the system of Equations 3 can be analytically inverted. Three input images are required and they have to be recorded at specific relative displacements between the two masks. One image is acquired

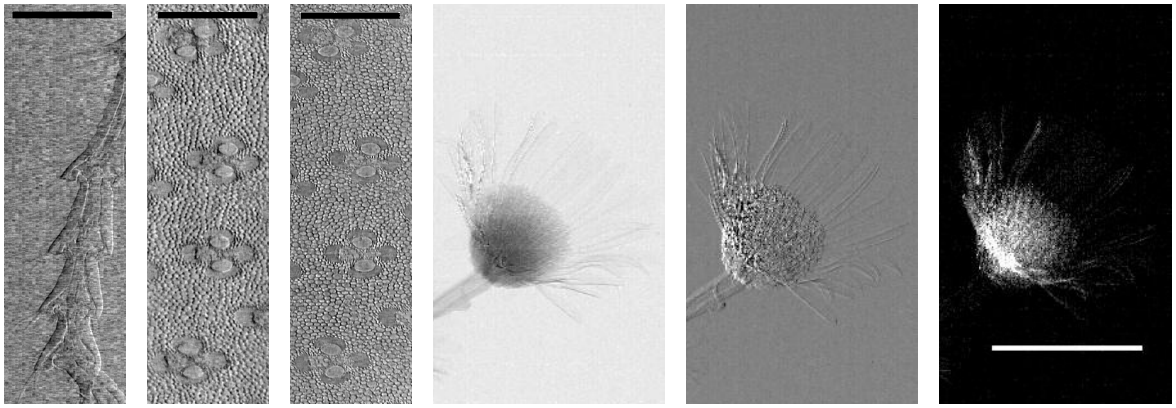

(a) (b) (c) (d) (e) (f)

Figure 2: Experimental images. (a) microscopic details of a ground beetle leg, intensity projection acquired at $\Delta\xi = 2$ μm. Differential phase (b) and transmission (c) images of bamboo wood micro-structure retrieved by using Equation 1. Scale bar is 500 μm in panels (a)-(c). Transmission (d), differential phase (e) and scattering (f) images of a flower (Chrysanthemum leucanthemum) obtained with the low magnification system of Figure 1(c). Scale bar is 1 cm for panels (d)-(f).

with the masks perfectly aligned ($\Delta\xi_2 = 0$) and the other two images are acquired with a symmetric displacement: ($\Delta\xi_1 = -\Delta\xi_3$). This produces the same reduction of intensity in the two symmetric positions, and it is achieved by displacing the masks by the same amount in opposite directions. The optimal value for $\Delta\xi_{1,3}$ typically depends on the specific imaging system design, a common choice is to displace the mask until the detected intensity reaches approximately 50% of the maximum (obtained at $\Delta\xi = 0$). If this simplified approximation is not valid for a particular experiment, more terms need to be retained in Equation 3 and the problem can still be solved by means of a numerical procedure as, for example, non-linear fitting.

3. Results

Figure 2 reports examples of experimental images acquired with laboratory implementations of EI. Panel (a) shows microscopic details of an insect leg as visualised by a single intensity projection image (I_L image, $\Delta\xi = 2$ μm). Panels (b) and (c) are the differential phase and transmission images of the micro-structure of bamboo wood (I_Δ/I_Σ and I_Σ). In this case, the $I_{L,R}$ images were recorded with a masks displacement of $\Delta\xi_1 = -\Delta\xi_2 = 2$ μm. This set-up featured a high X-ray beam energy (80 kVp on a tungsten target) and the insect leg can be effectively considered a pure phase object. Panels (d)-(f) show the transmission, differential phase and scattering images of a flower, respectively. This set-up used a lower energy: the X-ray spectrum generated by a molybdenum target operated at 40 kVp. The scale bar is 500 μm for panels (a)-(c) and 1 cm for panels (d)-(f).

Finally we present a comparison of a detail extracted from a breast tissue image as an example of a potential medical application. The specimen had a thickness of approximately 2.5 cm and was fixed in formalin. It was obtained from a mastectomy after informed consent and the study was approved by the local ethical regulatory bodies. Figure 3(a) shows the conventional, absorption-contrast based radiography while Figure 3(b) shows the EI one. The scale bar is 5 mm. It is apparent how the fibrous structure is more clearly represented in the EI image with respect to the conventional one. It should be noted that the EI image was obtained with a single exposure and both amplitude and phase effects are contributing to the image contrast. It

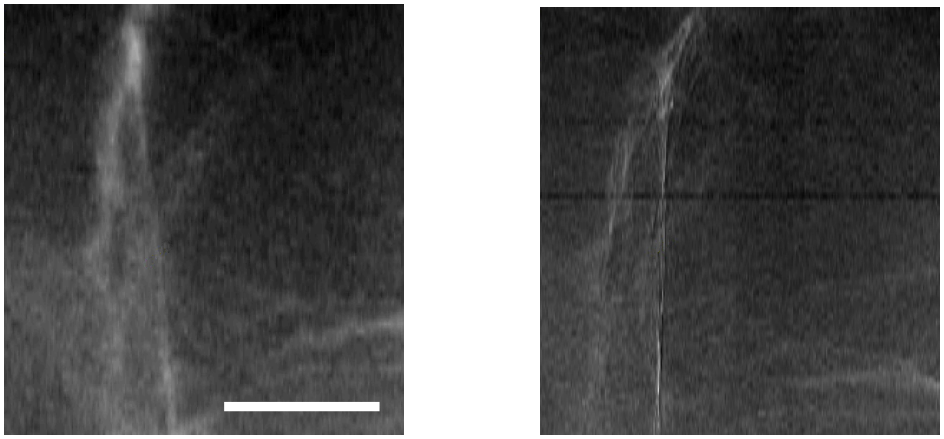

(a) (b)

Figure 3: Comparison between the standard (a) absorption-contrast based radiography and the (b) EI XPCI one. The scale bar is 5 mm. The specimen is breast tissue, approximately 2.5 cm thick. The detail of interest makes apparent how the fibrous structure is visible with much higher detail and contrast in the image obtained by means of the EI method, in comparison to conventional, absorption-based imaging.

was shown that with a laboratory EI system used in this configuration it is possible to perform low-dose mammography [30].

4. Conclusion

We reported and compared different implementations of the edge illumination for synchrotron- and laboratory-based X-ray phase contrast imaging applications. All these approaches are based on the use of an amplitude modulator that is placed before the sample. This is typically achieved by means of an absorbing slit, or mask, that structures the radiation field making the phase distortions introduced by the sample detectable. Different implementation regimes are available, resulting in widely ranging resolution and X-ray energy values, which can be tailored to specific applications in materials study, medical imaging and more.

Acknowledgements

This project was supported by the UK Engineering and Physical Sciences Research Council Grants EP/I022562/1 and EP/I021884/1. ME was supported by the Royal Academy of Engineering under the RAEng Research Fellowships scheme. PCD was supported by Marie Curie Career Integration Grant No. PCIG12-GA-2012-333990 within the Seventh Framework Programme of the European Union.

References

[1] Fitzgerald R 2000 *Physics Today* **53** 23–26
[2] Wilkins S, Nesterets Y I, Gureyev T, Mayo S, Pogany A and Stevenson A 2014 *Philosophical Transactions of the Royal Society of London A: Mathematical, Physical and Engineering Sciences* **372** 20130021
[3] Bravin A, Coan P and Suortti P 2013 *Physics in Medicine and Biology* **58** R1
[4] Bonse U and Hart M 1965 *Applied Physics Letters* **6** 155 –156
[5] Goetz K, Foerster E, Zaumseil P, Kalashnikov M P, Mikhailov I A, Sklizkov G V and Fedotov S I 1979 *Kvantovaia Elektronika Moscow* **6** 1037–1042
[6] Davis T J, Gao D, Gureyev T E, Stevenson A W and Wilkins S W 1995 *Nature* **373** 595–598

[7] Snigirev A, Snigireva I, Kohn V, Kuznetsov S and Schelokov I 1995 *Review of Scientific Instruments* **66** 5486–5492
[8] Ingal V N and Beliaevskaya E A 1995 *Journal of Physics D Applied Physics* **28** 2314–2317
[9] Wilkins S W, Gureyev T E, Gao D, Pogany A and Stevenson A W 1996 *Nature* **384** 335–338
[10] Chapman D, Thomlinson W, Johnston R E, Washburn D, Pisano E, Gmür N, Zhong Z, Menk R, Arfelli F and Sayers D 1997 *Physics in Medicine and Biology* **42** 2015–2025
[11] Clauser J F 1998 Us patent 5,812,629
[12] David C, Nohammer B, Solak H H and Ziegler E 2002 *Applied Physics Letters* **81** 3287–3289
[13] Momose A, Kawamoto S, Koyama I, Hamaishi Y, Takai K and Suzuki Y 2003 *Japanese Journal of Applied Physics* **42** L866
[14] Mayo S C and Sexton B 2004 *Optics Letters* **29** 866–868
[15] Pfeiffer F, Weitkamp T, Bunk O and David C 2006 *Nature Physics* **2** 258–261
[16] Wen H, Bennett E E, Hegedus M M and Rapacchi S 2009 *Radiology* **251** 910–918
[17] Morgan K S, Paganin D M and Siu K K W 2012 *Applied Physics Letters* **100** 124102
[18] Bérujon S, Ziegler E, Cerbino R and Peverini L 2012 *Physical Review Letters* **108** 158102
[19] Wen H, Gomella A A, Patel A, Lynch S K, Morgan N Y, Anderson S A, Bennett E E, Xiao X, Liu C and Wolfe D E 2013 *Nature Communications* **4**
[20] Olivo A, Arfelli F, Cantatore G, Longo R, Menk R H, Pani S, Prest M, Poropat P, Rigon L, Tromba G, Vallazza E and Castelli E 2001 *Medical Physics* **28** 1610–1619
[21] Olivo A and Speller R 2007 *Applied Physics Letters* **91** 074106 (pages 3)
[22] Endrizzi M, Vittoria F A, Diemoz P C, Lorenzo R, Speller R D, Wagner U H, Rau C, Robinson I K and Olivo A 2014 *Optics Letters* **39** 3332–3335
[23] Munro P R, Ignatyev K, Speller R D and Olivo A 2012 *Proc. Natl. Acad. Sci. USA* **109** 13922–13927
[24] Endrizzi M, Diemoz P C, Millard T P, Jones J L, Speller R D, Robinson I K and Olivo A 2014 *Applied Physics Letters* **104** 024106
[25] Marenzana M, Hagen C K, Borges P D N, Endrizzi M, Szafraniec M B, Ignatyev K and Olivo A 2012 *Physics in Medicine and Biology* **57** 8173
[26] Diemoz P C, Endrizzi M, Zapata C E, Pešić Z D, Rau C, Bravin A, Robinson I K and Olivo A 2013 *Physical Review Letters* **110**(13) 138105
[27] Diemoz P, Hagen C, Endrizzi M and Olivo A 2013 *Applied Physics Letters* **103** 244104
[28] Millard T P, Endrizzi M, Ignatyev K, Hagen C K, Munro P R T, Speller R D and Olivo A 2013 *Review of Scientific Instruments* **84** 083702
[29] Endrizzi M, Basta D and Olivo A 2015 *Applied Physics Letters* **107** 124103
[30] Olivo A, Gkoumas S, Endrizzi M, Hagen C K, Szafraniec M B, Diemoz P C, Munro P R T, Ignatyev K, Johnson B, Horrocks J A, Vinnicombe S J, Jones J L and Speller R D 2013 *Medical Physics* **40** 090701
[31] Hagen C, Munro P, Endrizzi M, Diemoz P and Olivo A 2014 *Medical Physics* **41** 070701
[32] Vittoria F A, Kallon G K, Basta D, Diemoz P C, Robinson I K, Olivo A and Endrizzi M 2015 *Applied Physics Letters* **106** 224102
[33] Vittoria F A, Endrizzi M, Diemoz P C, Wagner U H, Rau C, Robinson I K and Olivo A 2014 *Applied Physics Letters* **104** 134102
[34] Vittoria F A, Endrizzi M, Diemoz P C, Zamir A, Wagner U H, Rau C, Robinson I K and Olivo A 2015 *Scientific reports* **5**
[35] Endrizzi M, Vittoria F A, Kallon G, Basta D, Diemoz P C, Vincenzi A, Delogu P, Bellazzini R and Olivo A 2015 *Optics Express* **23** 16473–16480
[36] Munro P R, Hagen C K, Szafraniec M B and Olivo A 2013 *Optics Express* **21** 11187–11201
[37] Munro P R T and Olivo A 2013 *Phys. Rev. A* **87**(5) 053838
[38] Endrizzi M, Oliva P, Golosio B and Delogu P 2013 *Nucl. Instr. Meth. Phys. Res. A* **703** 26 – 32 ISSN 0168-9002